

Internal structure of spiral arms traced with [C II]: Unraveling the warm ionized medium, H I, and molecular emission lanes

T. Velusamy, W. D. Langer, P. F. Goldsmith, and J. L. Pineda

Jet Propulsion Laboratory, California Institute of Technology, 4800 Oak Grove Drive, Pasadena, CA 91109, USA
e-mail: Thangasamy.Velusamy@jpl.nasa.gov

Received 15 February 2015 / Accepted 9 April 2015

ABSTRACT

Context. The spiral arm tangencies are ideal lines of sight in which to determine the distribution of interstellar gas components in the spiral arms and study the influence of spiral density waves on the interarm gas in the Milky Way. [C II] emission in the tangencies delineates the warm ionized component and the photon-dominated regions and is thus an important probe of spiral arm structure and dynamics.

Aims. We aim to use [C II], H I, and ^{12}CO spectral line maps of the Crux, Norma, and Perseus tangencies to analyze the internal structure of the spiral arms in different gas layers.

Methods. We used [C II] l - V maps along with those for H I and ^{12}CO to derive the average spectral line intensity profiles over the longitudinal range of each tangency. Using the V_{LSR} of the emission features, we located the [C II], H I, and ^{12}CO emissions along a cross cut of the spiral arm. We used the [C II] velocity profile to identify the compressed warm ionized medium (WIM) in the spiral arm.

Results. We present a large-scale ($\sim 15^\circ$) position-velocity map of the Galactic plane in [C II] from $l = 326.6$ to 341.4 observed with *Herschel* HIFI. In the spectral line profiles at the tangencies, [C II] has two emission peaks, one associated with the compressed WIM and the other the molecular gas photon-dominated regions. When represented as a cut across the inner to outer edge of the spiral arm, the [C II]-WIM peak appears closest to the inner edge while ^{12}CO and [C II] associated with molecular gas are at the outermost edge. H I has broader emission with an intermediate peak located nearer to that of ^{12}CO .

Conclusions. The velocity-resolved spectral line data of the spiral arm tangencies unravel the internal structure in the arms locating the emission lanes within them. We interpret the excess [C II] near the tangent velocities as shock compression of the WIM induced by the spiral density waves and as the innermost edge of spiral arms. For the Norma and Perseus arms, we estimate widths of ~ 250 pc in [C II]-WIM and ~ 400 pc in ^{12}CO and overall spiral arm widths of ~ 500 pc in [C II] and ^{12}CO emissions; in H I the widths are ~ 400 pc and ~ 620 pc for Perseus and Norma, respectively. The electron densities in the WIM are $\sim 0.5 \text{ cm}^{-3}$, about an order of magnitude higher than the average for the disk. The enhanced electron density in the WIM is a result of compression of the WIM by the spiral density wave potential.

Key words. ISM: structure – Galaxy: structure – Galaxy: general – submillimeter: ISM – ISM: general

1. Introduction

The large-scale structure of spiral arms in the Milky Way has been a subject of great interest for understanding the dynamics of the Galaxy and for interpreting its properties. However, there have been long-standing disagreements about the number of arms and their physical parameters. While a majority of published papers favor a four-arm structure, others prefer a two-arm structure with a small pitch angle, allowing nearly two turns of the arms within the solar circle. In a series of papers, Vallée (2013, 2014a,b,c) attempted a statistical modeling analysis of all assembled recent positional data on the Milky Way's spiral arms and observed tangencies in a number of tracers such as CO, H I, methanol masers, hot and cold dust, and far-infrared (FIR) cooling lines, such as [C II]. The most recent version of his idealized synthesized Galactic map can be found in Vallée (2014a). Modeling the Galactic spiral structure is based mostly on the data at the spiral arm tangents as observed by different gas tracers and stars. However, each of these spiral arm tracers can occupy a separate lane, or layer, across an arm (e.g., Vallée 2014a,c), resulting in an inconsistency among the various models extracted from observational data.

In this paper we present new [C II] spectral line l - V maps of the Galactic plane covering $l = 326.6$ to 341.4 and $l = 304.9$ to 305.9 as obtained by *Herschel*¹ HIFI on-the-fly (OTF) mapping. These maps illuminate the structure of different gas components in the spiral arms. Using the [C II], H I and ^{12}CO maps of the Crux, Norma, and start of the Perseus tangencies, we derive the intensity profiles of their emissions across these spiral arms and quantify the relative displacement of the compressed warm ionized medium (WIM) and the atomic and molecular gas lanes with respect to the inner and outer edges of the arms. Our results reveal an evolutionary transition from the lowest to the highest density states induced by the spiral arm potential. This compressed WIM component traced by [C II] is distinct from the ionized gas in H II regions, which traces the spiral arms with characteristics similar to those of molecular gas traced by CO (cf. Vallée 2014a; Downes et al. 1980).

The spiral tangent regions (cf. Vallée 2008; Benjamin 2009) are ideal laboratories in which to study the interaction of the interstellar gas and spiral density waves in the Milky Way.

¹ *Herschel* is an ESA space observatory with science instruments provided by European-led Principal Investigator consortia and with important participation from NASA.

The tangents provide a unique viewing geometry with sufficiently long path lengths in relatively narrow velocity ranges to detect the diffuse WIM component traced by [C II] emission and to study its relationship to the neutral HI and molecular ^{12}CO gas components within spiral arms and the influence of spiral arm density waves on the interstellar medium (ISM).

COBE FIRAS observed strong [C II] and [N II] emission along the Galactic spiral arm tangencies, and Steiman-Cameron et al. (2010) fit the COBE results with four well-defined logarithmic spiral arms in the gaseous component of the ISM. However, COBE's 7° beam and spectrally unresolved lines preclude obtaining detailed information on the scale and properties of the gas within the spiral tangencies, nor can one use the COBE data to separate the emission that arises from the photon-dominated regions (PDRs) from that in the WIM. The HIFI Galactic Observations of Terahertz C+ (GOT C+) survey (Langer et al. 2010) of the Milky Way also detects the strongest [C II] emission near the spiral arm tangential directions (Pineda et al. 2013; Velusamy & Langer 2014). In the velocity-resolved HIFI spectra, Velusamy et al. (2012) separated the WIM component of the [C II] emission in velocity space from that in the molecular and neutral gas. They suggested that excitation by electrons in the WIM, with a density enhanced by the spiral arm potential, accounts for the low surface brightness [C II] excess observed at the tangent velocities along the Scutum-Crux spiral tangency. To determine whether a similar spatial and density distribution is a general property of Galactic spiral arms, it is important to observe the velocity structure of the [C II] emission in other spiral arm tangencies and compare it with the corresponding HI and ^{12}CO emissions.

Here we present a large-scale ($\sim 15^\circ$) position-velocity map of the Galactic plane in [C II] and derive the following characteristics of the spiral arm features: the relative locations of the peak emissions of the WIM, HI, and molecular gas lanes, including the PDRs, and the width of each layer. In addition, we use the [C II] emission to derive the mean electron density in the WIM. These results confirm our earlier conclusion (Velusamy et al. 2012) that in the velocity profile of [C II] emission at the Scutum tangency, the WIM and molecular gas components of [C II] are distinguished kinematically (appearing at well-separated velocities around the tangent velocity).

In the analysis presented here we use the fact that [C II] emission can arise in the three major constituents of the interstellar gas: fully or partially ionized gas (as in the WIM), neutral atomic gas (as in HI clouds), and H_2 molecular gas (such as CO clouds or PDRs) excited by electrons, H atoms, and H_2 molecules, respectively. These components are identified as demonstrated in the GOT C+ results in the velocity-resolved HIFI spectra (cf. Pineda et al. 2013; Langer et al. 2014; Velusamy & Langer 2014). Furthermore, Velusamy & Langer (2014) showed that in the inner Galaxy $\sim 60\%$ of the [C II] emission traces the H_2 molecular gas, while at least 30% of the [C II] traces the WIM. They also showed that emission in HI excited by H atoms is not a major contributor. To study spiral arm structure, we here identify two major [C II] components, one component that stems from the WIM, the other from PDRs. We find that in the spiral arm tangencies the [C II] spectral line data alone can be used to study the relative locations of the WIM and molecular gas PDR layers.

The outline of our paper is as follows. The observations are discussed in Sect. 2. In Sect. 3 we construct the spatial-velocity maps and compare the distributions of [C II] with HI and ^{12}CO and their relation to the spiral arms. In Sect. 4 we analyze the velocity structure of these gas components at the spiral arm

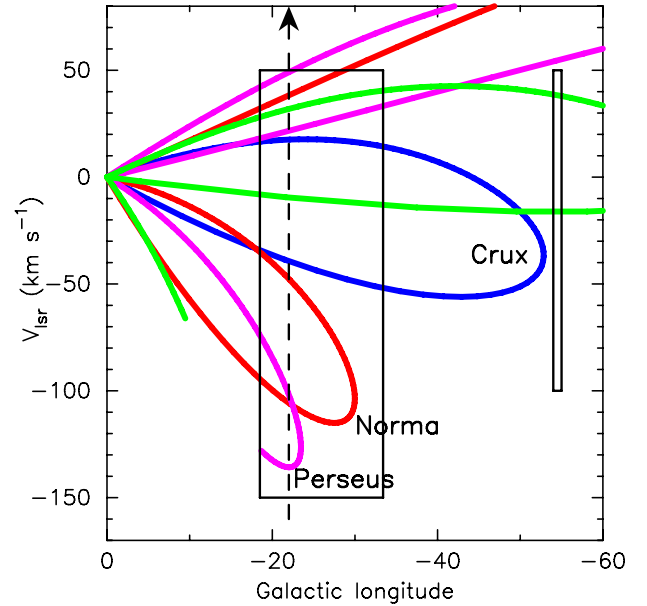


Fig. 1. Spiral arms in the fourth quadrant are represented in a V_{LSR} -longitude (V - l) plot, adapted from Vallée (2008): red: Norma-Cygnus; blue: Scutum-Crux; green: Sagittarius-Carina; magenta: Perseus. The rectangular boxes indicate the longitude extent in the Galactic plane at a latitude $b = 0^\circ$ of the HIFI [C II] spectral line map data presented here. Note that the maps cover the tangencies of the Norma, Crux, and start of the Perseus arms. The vertical dashed line represents a line of sight at a given longitude that intercepts multiple spiral arms, thus demonstrating the need for velocity-resolved spectral line data to separate them.

tangencies and use it to infer the relative locations of the different gas lanes within the spiral arm. Note that in discussing the internal structure of the spiral arms we refer to the emission layers of the gas tracers as lanes, analogous to the terminology used in external spiral galaxies. We also derive the average electron density in the WIM using the [C II] emission and a radiative transfer model. We summarize our results in Sect. 5.

2. Observations

The longitudinal and velocity coverage of the [C II] observations at a latitude $b = 0^\circ$ presented here are summarized in Fig. 1. We also show the velocity-longitude relationship of the spiral arm in a schematic view. All [C II] spectral line map observations were made with the high spectral resolution HIFI (de Graauw et al. 2010) instrument onboard *Herschel* (Pilbratt et al. 2010). These observations were taken between October 2011 and February 2012. We used 37 OTF scans for the large-scale [C II] map of the Galactic plane (at $b = 0^\circ$), covering a 15° range in longitude between $326^\circ.6$ and $341^\circ.4$, which include the Norma and Perseus tangencies. The observations of the fine-structure transition of C^+ ($^2\text{P}_{3/2}$ - $^2\text{P}_{1/2}$) at 1900.5369 GHz were made with the HIFI band 7b using the wideband spectrometer (WBS). Each OTF scan was taken along the Galactic longitude at latitude $b = 0^\circ$ and was 24 arcmin long. For the Crux tangency two OTF longitude scan data were used: (i) one 24 arcmin long centered at $l = 305^\circ.1$ and $b = 0^\circ$ (note an earlier version of this map was presented in Velusamy & Langer (2014) and it is included here for completeness in the analysis of the tangencies); and (ii) a shorter 6 arcmin long scan centered at $l = 305^\circ.76$ and $b = 0^\circ.15$. All HIFI OTF scans were made in the LOAD-CHOP mode using a reference off-source position about 2 degrees away in latitude

(at $b = 1^\circ 9$). However, we did not use off-source data (see below). All the 24 arcmin long OTF scans were sampled every 40 arcsec and the shorter scan every 20 arcsec. The total duration of each OTF scan was typically ~ 2000 s, which only provides a short integration time on each spectrum (pixel). Thus the rms (0.22 K in T_{mb}) in the final maps with an $80''$ beam and 2 km s^{-1} wide channels in the OTF spectra is much larger than the rms in the HIFI spectra observed in the HPOINT mode, for example, in the GOT C+ data. The observations for the Crux tangency used longer integrations.

We processed the OTF scan map data following the procedure discussed in Velusamy & Langer (2014). The [C II] spectral line data were taken with HIFI Band 7, which used hot electron bolometer (HEB) detectors. These HEBs produced strong electrical standing waves with characteristic periods of ~ 320 MHz that depend on the signal power. The HIPE Level 2 [C II] spectra show these residual waves. We found that applying the task *fitHifiFringe*² to the Level 2 data produced satisfactory baselines. However, removal of the HEB standing waves has remained a challenge up until the recent release of HIPE-12, which includes a new tool, *hebCorrection*³, to remove the standing waves in the raw spectral data by matching the standing-wave patterns (appropriate to the power level) in each integration using a database of spectra at different power levels (see *Herschel* Science Center (HSC) HIPE-12 release document for details). We used this HSC script to apply *hebCorrection* to create the final pipeline-mapping products presented here. Following one of the procedures suggested by David Teyssier at the HSC, the OTF map data presented here were processed by re-doing the pipeline without off source subtraction to produce Level 1 data. The *hebCorrection* was then applied to these new Level 1 data. The fact that *hebCorrection* subtracts the matching standing-wave patterns from a large database of spectra eliminates the need for off-source subtraction. In our analysis the processed spectral data are therefore free from any off-source contamination. While fitting the HEB waves, we also used the feature in the *hebCorrection* script to exclude the IF frequencies with strong [C II] emissions. Finally, the Level 2 data were produced from the HEB-corrected Level 1 data.

From Level 2 data the [C II] maps were made as spectral line cubes using the standard mapping scripts in HIPE. Any residual HEB and optical standing waves in the reprocessed Level 2 data were minimized further by applying *fitHifiFringe* to the gridded spectral data (we took the additional precaution in *fitHifiFringe* of disabling *DoAverage* so as not to bias the spectral line window). The H- and V-polarization data were processed separately and were only combined after applying *fitHifiFringe* to the gridded data. This approach minimizes the standing-wave residues in the scan maps by taking into account the standing-wave differences between H- and V-polarization.

All OTF scan map data were reprocessed and analyzed in HIPE 12.1, as described above, to create spectral line data cubes. We then used the processed spectral line data cubes to make longitude-velocity (l - V) maps of the [C II] emission as a function of the longitude range in each of the 39 OTF observations. For HIFI observations we used the Wide Band Spectrometer (WBS) with a spectral resolution of 1.1 MHz for all the scan maps. The final l - V maps presented here were restored with a velocity resolution of 2 km s^{-1} . At 1.9 THz the angular resolution

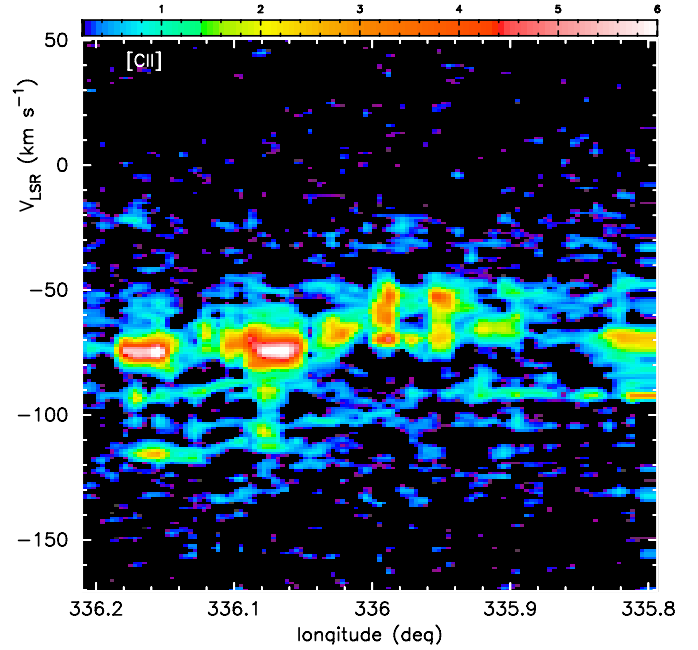


Fig. 2. Examples of a [C II] OTF longitudinal scan l - V map centered at $l = 336^\circ 0$ and $b = 0^\circ 0$. The intensities are in main-beam antenna temperature (T_{mb}) with values indicated by the color wedge at the top. A square-root color stretch is used to bring out the low-brightness emission features. The velocity resolution in all maps is 2 km s^{-1} , and the restored beam size in longitude is $80''$.

of the *Herschel* telescope is $12''$, but the [C II] OTF observations used $40''$ sampling. Such fast scanning results in heavily undersampled scans broaden the effective beam size along the scan direction (Mangum et al. 2007). Therefore all [C II] maps were restored with effective beam sizes corresponding to twice the sampling interval along the scan direction ($\sim 80''$). Figure 2 shows an example of a l - V map reconstructed using the map data processed in HIPE 12.1 for a single OTF scan map observed at longitude $l = 336^\circ 0$.

To compare the distribution of atomic and molecular gas with the ionized gas, we used the ^{12}CO and HI data in the southern Galactic plane surveys available in the public archives. The $^{12}\text{CO}(1-0)$ data were taken from the Three-mm Ultimate Mopra Milky Way Survey⁴ (ThrUMMS) observed with the 22m Mopra telescope (Barnes et al. 2011). The HI data were taken from the Southern Galactic Plane Survey (SGPS) observed with the Australia Telescope Compact Array (McClure-Griffiths et al. 2005). Although the Park HIPASS Galactic plane map of the H 166, 167, and 168 α radio recombination lines (RRL) is now available (Alves et al. 2015), its low-velocity resolution ($\sim 20 \text{ km s}^{-1}$) precludes using it for the analysis presented here. Furthermore, as the H II regions are associated with star formation and dense molecular gas (e.g., Anderson et al. 2009), the RRL emission from H II regions probably does not add more information to the spiral arm structures than is already traced by ^{12}CO .

3. Results

In this section we present the l - V emission maps and analyze the structure of the different gas components. We use a schematic of the expected relationship between velocity (V_{LSR}) and location

² http://herschel.esac.esa.int/hcss-doc-12.0/index.jsp#hifi_um:hifi\discretionary-um Sect. 10.3.2

³ http://herschel.esac.esa.int/hcss-doc-12.0/index.jsp#hifi_um:hifi\discretionary-um Sect. 10.4.5

⁴ www.astro.ufl.edu/thrumms

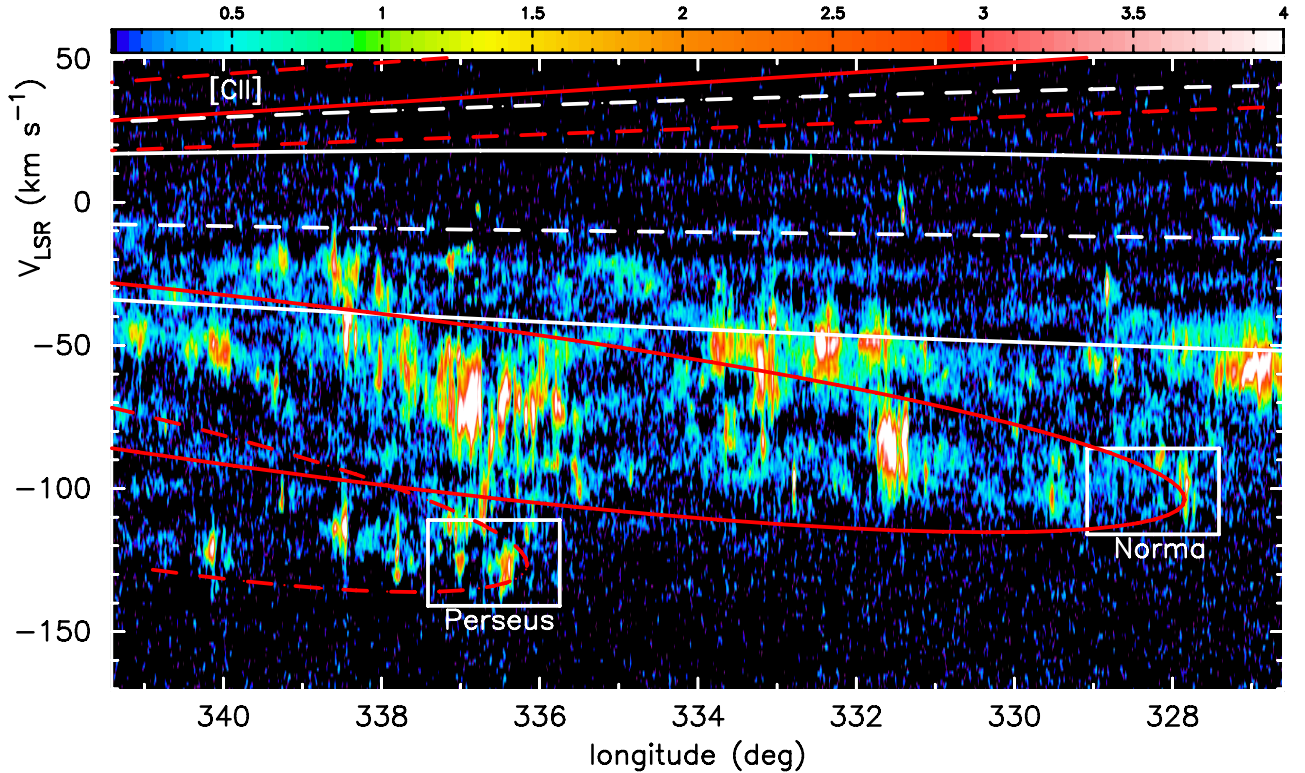


Fig. 3. [C II] longitude-velocity (l - V) map covering $\sim 15^\circ$ in longitude over the range $l = 326.6$ to 341.4 at $b = 0.0$. The intensities are in main-beam antenna temperature (T_{mb}) with values indicated by the color wedge. A square-root color stretch is used to bring out the low-brightness emission features. The velocity resolution in all maps is 2 km s^{-1} and the beam size along the longitudinal direction is $80''$. A sketch of the spiral arms in the fourth quadrant, adopted from Vallée (2008), is overlaid and indicated in the following colors: red-solid: Norma-Cygnus; white-solid: Scutum-Crux; white-dashed: Sagittarius-Carina; red-dashed: Perseus. The rectangular boxes indicate the extent of the spiral tangencies as labeled.

with respect to Galactic center to guide the analysis of the gas lane profile across the arm. We show that the emissions reveal an orderly change in gas components across the arms, leading from the least dense WIM to the densest molecular clouds.

3.1. Longitude-velocity maps

We stitched all the individual OTF maps (an example is shown in Fig. 2) within the longitude range 326.6 to 341.4 to create a single longitude-velocity map that includes the Perseus and Norma tangencies. This l - V map is shown in Fig. 3. An l - V representation of the spiral arms is overlaid on the [C II] map. Note that strong [C II] emissions are seen in the tangencies (denoted by the boxes in Fig. 3) as seen in the GOT C+ survey data (Pineda et al. 2013; Velusamy & Langer 2014) and COBE data (Steiman-Cameron et al. 2010). However, the rest of the spiral arm trajectories show poor correspondence with the brightness of [C II] emission, probably because of the uncertainties in the model parameters (e.g., pitch angle) used for the spiral arms. We assembled the l - V maps that match the [C II] map for the $^{12}\text{CO}(1-0)$ (Fig. 4) and HI (Fig. 5) maps using the Mopra ThrUMMS survey and SGPS data. Note that the intensities for ThrUMMS $^{12}\text{CO}(1-0)$ data are uncorrected for main-beam efficiency (Ladd et al. 2005; Barnes et al. 2011).

The [C II] maps in Fig. 3 contain in addition to information about the tangency a rich data set on [C II] emission in the diffuse gas, the molecular gas, and PDRs; these properties have been analyzed in detail for a sparse galactic sample using the GOT C+ data base (Pineda et al. 2013; Langer et al. 2014; Velusamy & Langer 2014). However, the continuous longitude coverage

in the data presented here offers a better opportunity for studying the Galactic spiral structure and the internal structure of the arms. In principle, it is possible to derive a 2D spatial-intensity map of this portion of the Galaxy using the kinematic distances for each velocity feature in the maps. However, such a study is subject to the near-far-distance ambiguities inherent in lines of sight inside the solar circle (see discussion in Velusamy & Langer 2014), except along the tangencies. The tangencies offer a unique geometry in which to study kinematics of the interstellar gas without the distance ambiguity. Furthermore, the tangential longitudes provide the longest path length along the line of sight through a cross section of the spiral arm, thus making it easier to detect weak [C II] emission from the WIM and the molecular gas. In this paper we limit our analysis to the [C II] emission in tangencies and compare it with those of HI and ^{12}CO to understand the structure of the spiral arms in different ISM components.

3.2. Tangent emission-velocity profiles

In Fig. 6 we show a schematic model of the internal structure of a spiral arm based on the results of Vallée (2014a) and Velusamy et al. (2012), using the Norma tangency as an example. Figure 6a illustrates how the emission for the tangency probes the lanes seen in different tracers. In Vallée's schematic (see his Fig. 5), both HI and [C II] emissions occur displaced from ^{12}CO toward the inner edge (on the near side of the Galactic center). In Vallée's sketch the displacement of [C II] with respect to ^{12}CO is based on the COBE data (Steiman-Cameron et al. 2010). However, in the velocity-resolved HIFI data for

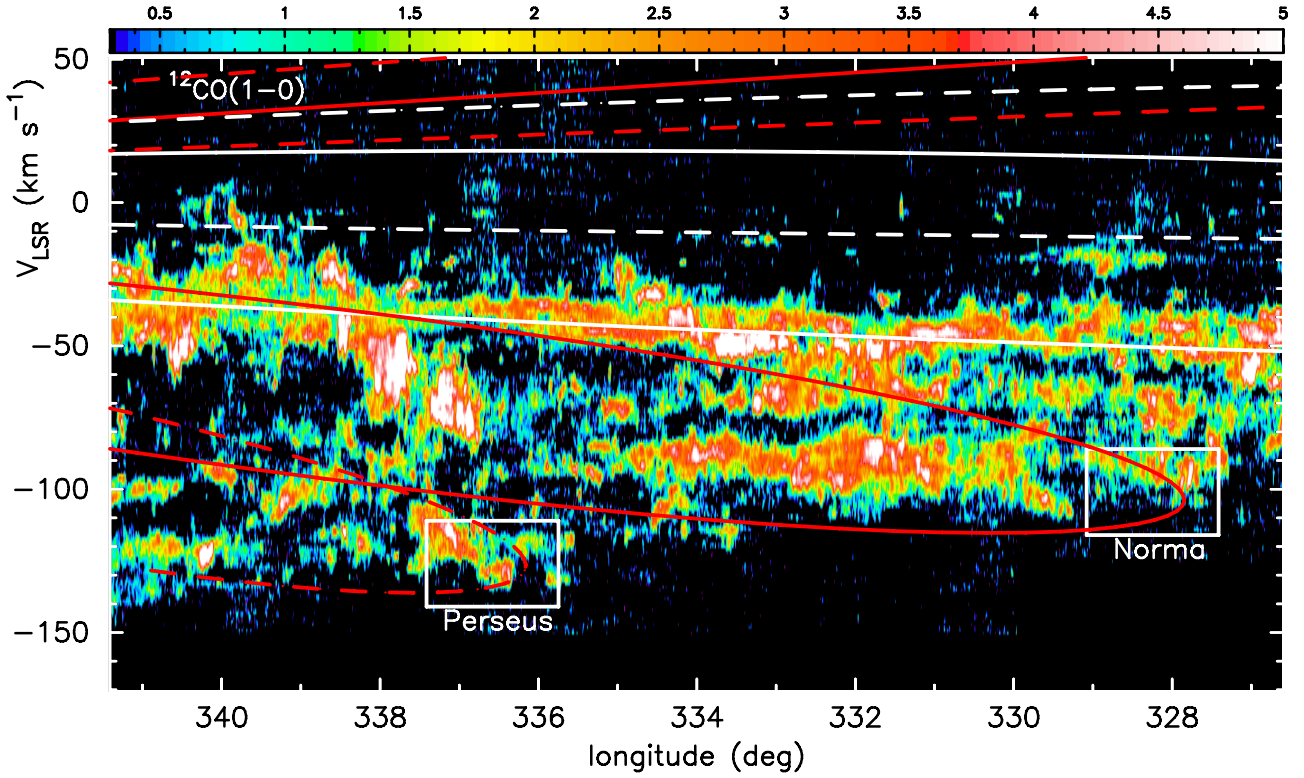


Fig. 4. $^{12}\text{CO}(1-0)$ longitude-velocity (l - V) map covering $\sim 15^\circ$ in longitude over the range $l = 326:6$ to $341:4$ at $b = 0:0$. The $^{12}\text{CO}(1-0)$ data are taken from Mopra ThrUMMS survey (Barnes et al. 2011). See the caption of Fig. 3 for the color labels.

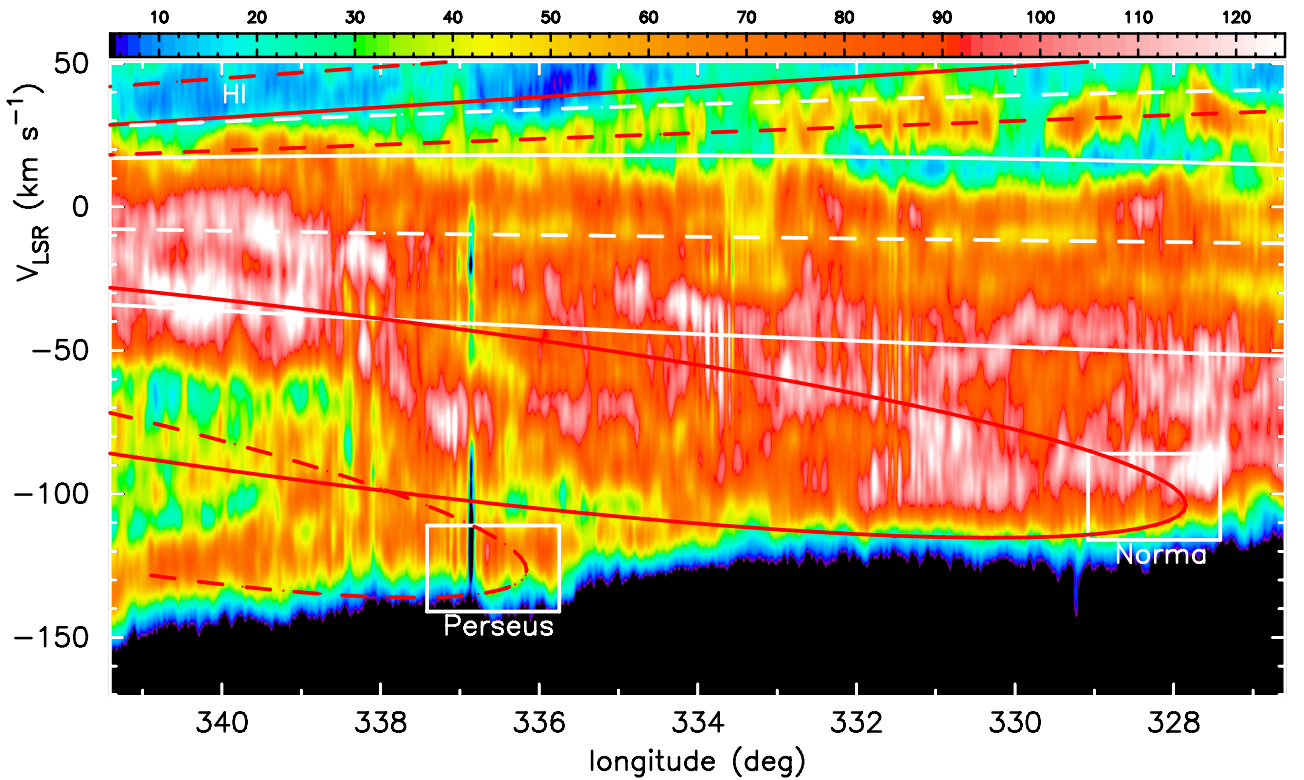


Fig. 5. HI longitude-velocity (l - V) map covering the $\sim 15^\circ$ range in longitude $l = 326:6$ to $341:4$ at $b = 0:0$. The HI data are taken from the SGPS survey (McClure-Griffiths et al. 2005). See the caption of Fig. 3 for the color labels.

the Scutum tangency (Velusamy et al. 2012), the WIM component of [C II] emission occurs near the inner edge, while that associated with molecular gas and PDRs is coincident with

^{12}CO emission. The boxed region in Fig. 6a represents the area in the tangency over which the emission spectra are computed. The expected velocity profiles at the tangency, relative to

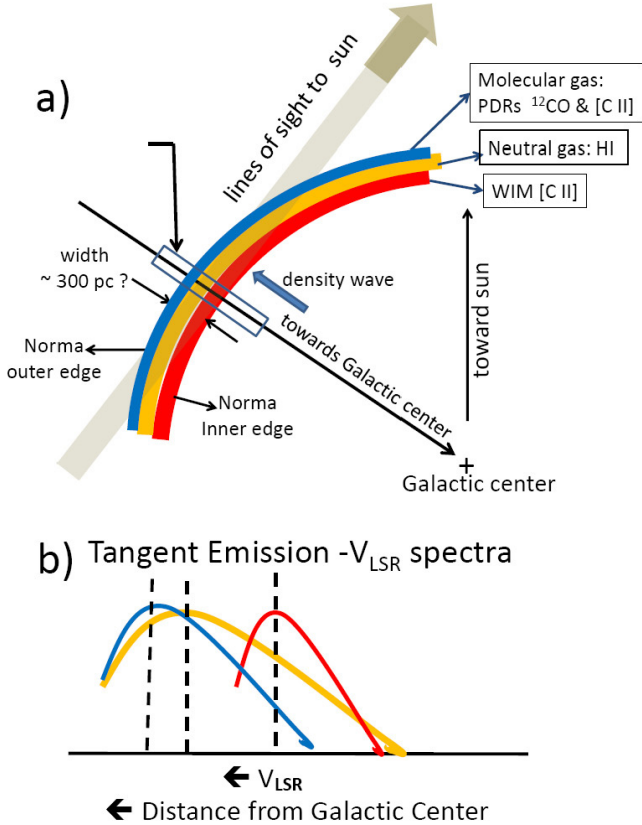


Fig. 6. **a)** Schematic view of the Norma spiral arm tangency. The emissions (distinguished by color) tracing the spiral arm are shown as a cross cut of the layers from the inner to outer edges (adapted from Figs. 2 and 3 in Vallée 2014a). **b)** A sketch indicating the velocity (V_{LSR}) structure of the corresponding spectral line intensities near the tangency for each layer. Note that this cartoon is intended to be a schematic and is not to scale.

the other emission layers, are shown schematically in Fig. 6b and can be compared with the actual observed velocity profiles for each tracer in the maps in Figs. 3 to 5. Thus we can examine the location of the respective emission layers relative to each other within each spiral arm by analyzing the velocity profiles of different gas tracers.

The trajectory of each spiral arm radial velocity (V_{LSR}) as a function of Galactic longitude is shown as a line in the l - V maps. In reality, however, it is expected to be much broader and complex. Obviously, there is no single unique value of the longitude that can be assigned as a tangency. Furthermore, the longitudes listed in the literature (e.g., Vallée 2014a) often correspond to data averaged over a wider range of Galactic latitudes. But the l - V maps presented here are all in the Galactic plane ($b = 0^\circ$) observed with narrow beam sizes in latitude ($12''$, $33''$, and $150''$ for [C II], ^{12}CO , and HI, respectively). In the maps in Figs. 3 to 5 we refer to a range of longitudes for each spiral tangency as indicated by the box sizes.

Using the l - V maps in Figs. 3 to 5, we averaged the emissions within a 2° and 2.5° longitude range for the Perseus and Norma tangencies, respectively, and in all observed longitudes for the Crux tangency. The resulting averaged spectra are plotted in Figs. 7b and 8b. Note that the ^{12}CO spectra shown have new baselines fitted to the map data in Fig. 4. For clarity we limited the velocity range to only cover the tangencies. Furthermore, the intensity scale for each spectrum was adjusted such that the highest value corresponds to its peak brightness listed in Table 1.

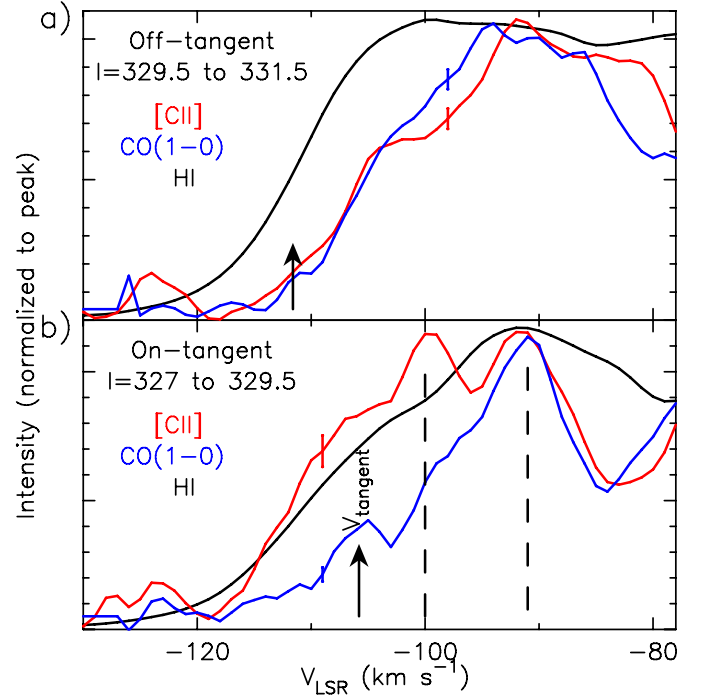


Fig. 7. Norma tangency spectra. The [C II], HI, and ^{12}CO emission spectra are plotted against velocity (V_{LSR}). Each panel shows the spectra for the indicated longitude ranges. Note that the intensity scale is normalized to the peak emission within the velocity range. The corresponding 1σ error bars are indicated on the [C II] and ^{12}CO spectra. The tangent velocity is marked on each panel by a vertical arrow. Panel **a)**: Off-tangent. Panel **b)**: On-tangent. The dashed lines indicate the V_{LSR} shift between the [C II] and ^{12}CO peaks.

The tangent velocity is indicated in the spectra in each panel in Figs. 7, 8, and 10 to provide a reference to the V_{LSR} velocities. The tangent velocities were estimated using the mean longitude and assuming Galactic rotational velocity (220 km s^{-1}) at the tangent points (cf. Levine et al. 2008). We note that the tangent velocity varies from panel to panel, corresponding to its longitude range. The [C II] spectra of the tangencies show remarkably distinct differences compared to spectra of HI or ^{12}CO . [C II], unlike HI or ^{12}CO , shows a clear emission peak near the tangent velocity, well separated from the HI and ^{12}CO peaks. To bring out the uniqueness of these differences in the tangencies, we compare in Figs. 7 and 8 the spectra at tangencies (labeled “On-tangent”) with those at neighboring longitudes (labeled “Off-tangent”). As discussed below, only the spectra at the tangencies show the excess [C II] emission peak at more negative velocities. As illustrated in the schematic in Fig. 6, it is possible to individually delineate the emission layers or the lanes, highlighting the internal structure of the spiral arms, for [C II] in both the WIM and the PDRs, as well as that of molecular gas in ^{12}CO and atomic gas in HI. The characteristics of the observed velocity profiles in each tangency are summarized Table 1.

3.2.1. Norma tangency

The Norma tangency has been determined as 328° for ^{12}CO (Bronfman et al. 2000) and HI (Engelmaier & Gerhard 1999), 329° for $60 \mu\text{m}$ dust (Bloemen et al. 1990), and 332° for $870 \mu\text{m}$ dust (Beuther et al. 2012). García et al. (2014) assigned tangent directions to the Crux (Centaurus), Norma, and 3 kpc expanding arms of 310° , 330° , and 338° , respectively, by fitting a

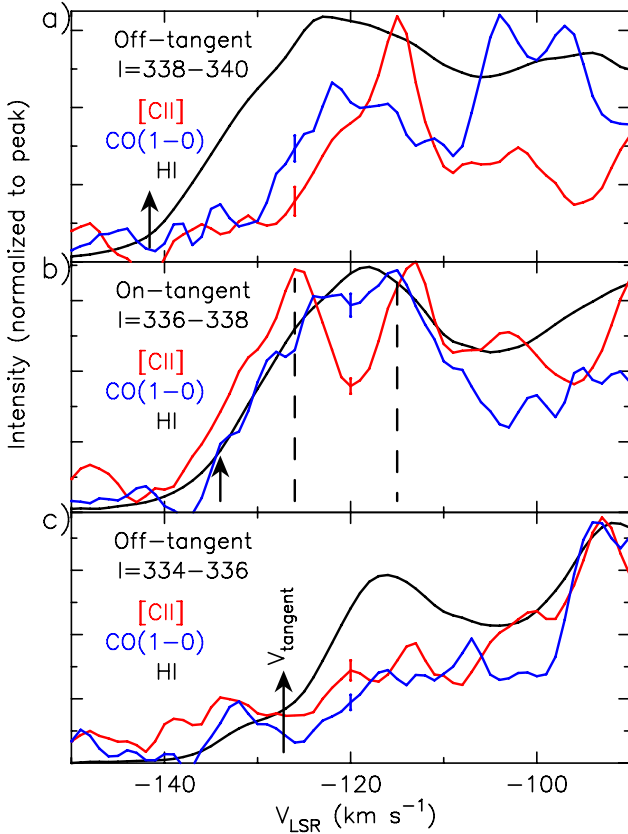


Fig. 8. Spectra for the location of the start of the Perseus tangency. The caption is same as for Fig. 7. Panels **a**) and **c**): Off-tangent. Panel **b**): On-tangent. The dashed lines indicate the shifted V_{LSR} of peak emission of the [C II] and ^{12}CO .

logarithmic spiral arm model to the distribution of giant molecular clouds (GMCs). As discussed above, the detection of [C II] from the WIM is strongest along the tangencies and thus is a good discriminator of the tangent direction of a spiral arm. The emission profiles shown in Fig. 7 therefore provide strong evidence that the longitude of the tangent direction is well constrained to $l < 329.5$. The ^{12}CO emission shows a small peak near the tangent velocity in the on-tangent spectrum. However, this feature is relatively weak when compared to the prominent emission seen in [C II].

3.2.2. Start of Perseus tangency

The tangency at the start of the Perseus arm has been determined as 336° for ^{12}CO (Bronfman et al. 2000), 338° for the [C II] and [N II] FIR lines (Steiman-Cameron et al. 2010), and 338° for $870 \mu\text{m}$ dust (Beuther et al. 2012). Green et al. (2011) suggested that part of the Perseus arm might harbor some of the methanol masers found toward the tangent direction of the 3 kpc expanding arm. According to the spiral arm model of Russeil (2003), the starting point of the Perseus arm would be found in the region between the Norma and the 3 kpc expanding arms. Although there are some doubts about this longitude being the start of the Perseus arm (cf. Green et al. 2011), we adopted the longitude range $l = 336^\circ\text{--}338^\circ$ as the start of the Perseus arm following the work of Vallée (2014a). The emission profiles in Fig. 8 clearly show the detection of a tangent direction in this longitude range, as seen by the strong [C II]–WIM emission compared to the weaker [C II] emission in the neighboring longitudes on either side.

Table 1. Observed spiral arm parameters at the Perseus, Norma, and Crux tangencies.

Spiral arm tangency	Perseus	Norma	Crux ¹
longitude $l =$	$336^\circ\text{0}'\text{--}338^\circ\text{0}'$	$327^\circ\text{0}'\text{--}329^\circ\text{5}'$	$304^\circ\text{9}'\text{--}305^\circ\text{9}'$
Emissions: V_{peak} (km s^{-1})			
[C II]–WIM	–126	–99.5	–52
[C II] (molecular) ²	–113	–91.5	–35
^{12}CO	–117	–91	–32.5
HI	–118	–92	–38
Emissions: Peak brightness T_{mb}(K)			
[C II]–WIM	0.56	0.35	~0.94
[C II](molecular)	0.58	0.35	5.0
^{12}CO ³	2.03	2.12	4.8
HI	70	118	106
Galactocentric distance of emission layers (kpc)⁴			
[C II]–WIM	3.45	4.57	6.59
^{12}CO (mid-plane)	3.60	4.76	7.20
HI	3.58	4.74	7.01

Notes. ⁽¹⁾ This longitude range is offset from the true tangency by $\sim 2^\circ$. Our data are only available for this longitude range. ⁽²⁾ This identification with H_2 gas is used just to distinguish it from the compressed WIM. However, in addition to excitation by H_2 , this component may include some [C II] excited by atomic H or electrons in the diffuse ionized medium. ⁽³⁾ Uncorrected for main-beam efficiency. ⁽⁴⁾ From the Galactic center as determined from the V_{LSR} and Galactic rotation velocity.

3.2.3. Crux tangency

Vallée (2014a) listed the Crux⁵ tangency as between $l = 309^\circ$ and 311° in different tracers with CO at $l = 309^\circ$ (Bronfman et al. 2000) and dust at $l = 311^\circ$ (Drimmel 2000; Bloemen et al. 1990; Beuther et al. 2012). However, using the GLIMPSE source counts, Benjamin et al. (2005) and Churchwell et al. (2009) placed the Crux tangency within a broader longitude range $306^\circ < l < 313^\circ$. Furthermore, it has been suggested that the Crux tangency provides an ideal testing ground for models of spiral density wave theory (Benjamin 2008), as the $l = 302^\circ$ to 313° direction is known to have several distinct anomalies, including large deviations in the HI velocity field (McClure-Griffiths & Dickey 2007) and a clear magnetic field reversal (Brown et al. 2007). Although we do not have a complete map of this region, it is of sufficient interest that we present a partial map covering $l = 304.9^\circ$ and 305.9° , which is close to the Crux tangency. This partial l - V map, which comes from another of our [C II] *Herschel* projects, is shown in Fig. 9 along with the corresponding ^{12}CO and HI maps. Note that the velocity range for the emission in the ^{12}CO map is much narrower than in the [C II] map; this difference is indicative of a broader diffuse emission component in [C II].

The emission profiles for the Crux tangent region shown in Fig. 10 are very similar to those observed for the Scutum tangency (Velusamy et al. 2012). The [C II] emission shows a clear excess beyond the tangent velocity. However, unlike the Norma or Perseus tangencies, we do not detect a resolved [C II] emission peak, and the WIM component appears as an enhanced

⁵ Also referred to as Centaurus as it appears in this constellation.

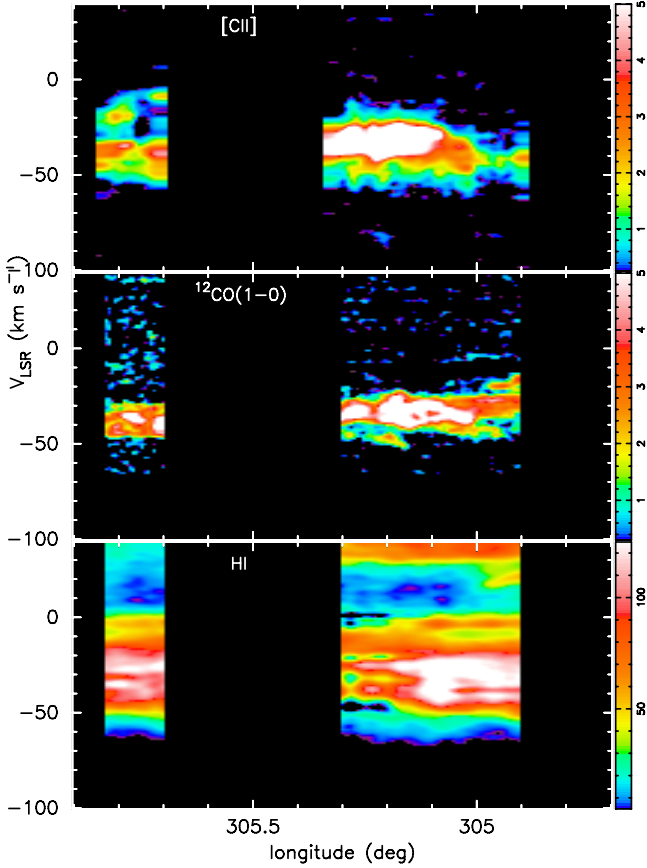


Fig. 9. Longitude-velocity (l - V) map covering part of the Crux tangency between longitudes $l = 304.9$ to 305.9 . **a)** HIFI [C II] maps covered in two OTF longitude scans centered at $l = 305.1^\circ$ and 305.76° at $b = 0.0$ and 0.15 , respectively. **b)** The corresponding ^{12}CO map from the Mopra ThrUMMS survey. **c)** The corresponding HI map from SGPS survey. This map region is off to the right of the l - V trajectory of the Crux tangency, as shown in Fig. 1 (see text). See also the caption of Fig. 3 for details on the display.

emission shoulder under the HI emission profile. This difference may be partly due to the fact that the longitude range of these maps is well outside the nominal tangent direction and may also be due to much stronger emissions seen in both [C II] and ^{12}CO close to the tangent velocity. Nevertheless, the detection of the [C II] excess associated with low HI and little or no ^{12}CO and its similarity to the results for the Scutum tangency strongly favor its interpretation as the WIM. This detection of WIM in the longitudes $l = 304.9$ to 305.9 indicates that the Crux tangency probably is much broader ($l = 302^\circ$ to 313°) in longitude than the other arms, as was indicated by the analysis of star counts in the *Spitzer* data (Benjamin et al. 2005).

4. Discussion

The spectra in Figs. 7, 8, and 10 clearly highlight the exceptional characteristics of the [C II] emission at the tangencies. These are as follows:

1. At the highest velocities near the tangent velocity, only [C II] shows a peak in emission, while there is little or no ^{12}CO and HI is weak, but increasing slowly with velocity. (The low-intensity ^{12}CO peak near the tangent velocity in Fig. 7 is less prominent when compared to the dominant [C II] emission).

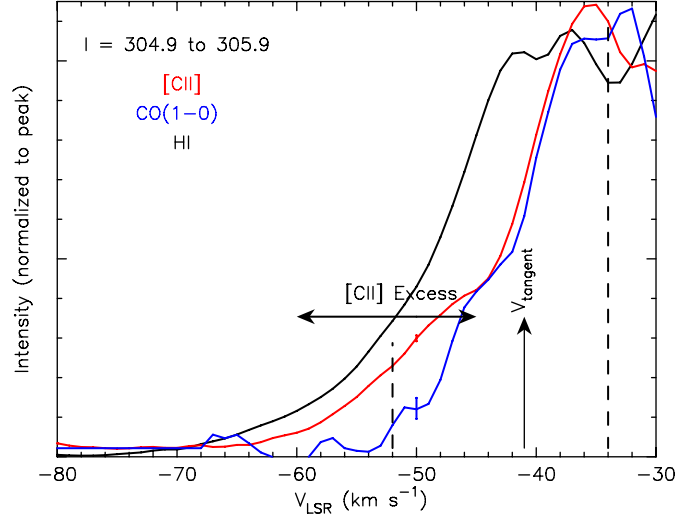


Fig. 10. Crux tangency emission spectra showing [C II], HI, and ^{12}CO emission plotted against velocity (V_{LSR}). The spectra are averaged over the longitude range indicated. Note that the intensity scale is normalized to the peak emission within the velocity range. The corresponding $1\text{-}\sigma$ error bars are indicated in the [C II] and ^{12}CO spectra at $V_{\text{LSR}} = 50 \text{ km s}^{-1}$. The tangent velocity is also marked. The dashed lines indicate the [C II] excess beyond the tangent velocity and ^{12}CO peak in the spectra.

2. The velocity of the [C II] peak near the tangent velocity corresponds to the radial distance closest to the Galactic center. Therefore it is near the inner edge of the spiral arm, representing the onset of the spiral arm feature.
3. The peak emissions for HI and ^{12}CO appear at still higher velocities than for the first [C II] peak corresponding to distances away from the inner edge.
4. [C II] emission shows two peaks: one near or beyond the tangent velocity representing the WIM component traced by [C II], and the second corresponding to the molecular gas traced by [C II] observed in association with ^{12}CO arising from the PDRs of the CO clouds.
5. The observed velocity profiles are consistent with the schematic shown in Fig. 6 for the internal structure of the spiral arm.

The anomalous excess [C II] emission in the velocity profiles for all the spiral arm tangencies represents the direct unambiguous detection of the large-scale Galactic diffuse ionized gas (WIM) through its $158 \mu\text{m}$ [C II] line emission. Our *Herschel* HIFI detection of the diffuse ionized gas provides detailed spatial and kinematic information on the nature of this gas component in the spiral arms that has not been possible with previous [C II] surveys. For example, in contrast to the direct detection of the WIM in [C II] in our HIFI data, the deduction of the WIM component in the COBE [C II] data (Steiman-Cameron et al. 2010) is indirect because it depends on using the [N II] intensities to separate the fraction of [C II] intensity from the WIM from other gas components, and is model dependent.

We can be certain that the [C II] emissions near the tangent velocity come from the highly ionized WIM and are the result of electron excitation of C^+ and not from H atom excitation from diffuse HI clouds (warm neutral medium or cold neutral medium) for the following reasons, as first noted in our earlier study of the WIM in the Scutum-Crux arm (Velusamy et al. 2012; Velusamy & Langer 2014). In the spectra in Figs. 7 and 8, the HI emission at the lowest velocities (near the left around

the tangent velocities) is only seen along with [C II] for the longitudes of tangent directions that are identified to have [C II] in the WIM (Figs. 7b and 8b). However, in all other longitude directions (Figs. 7a, 8a, and 8c), strong HI emission is seen with little or no associated [C II] emission. If H atom collisional excitation contributed to any of the [C II] emission we identify as coming from the WIM, then we should have seen [C II] associated with the HI emission for all longitudes in Figs. 7 and 8. However, we see none. It is even more unlikely that [C II] excess in the tangents is associated with CO-dark H₂ gas. In the velocity profiles of the On-tangent regions the [C II] emission starts appearing at lower velocities than ¹²CO. In contrast, in the velocity profiles of the Off-tangent regions both [C II] and ¹²CO begin to appear simultaneously. Considering the relatively weak ¹²CO emission, we only expect that a small fraction of the [C II] excess at the tangent is excited by H₂ molecules, if at all. Therefore we assume that [C II] excess is dominated by contribution from excitation by electrons.

The detection of WIM emission from our HIFI OTF survey is surprising because the average electron density in the WIM throughout the disk, $\sim a \text{ few } \times 10^{-2} \text{ cm}^{-3}$, is too low to result in detectable [C II] emission at the sensitivity of our HIFI OTF maps. Our explanation for the [C II] emission detected in our survey is that it originates from denser ionized gas along the inner edge of the spiral arms that has been compressed by the spiral density wave shocks (Fig 6), as previously discussed by Velusamy et al. (2012) for the Scutum-Crux arm. Indeed, as shown below, the electron density is significantly higher in the spiral arm WIM than between the arms. Below we derive the physical characteristics of the spiral arm gas lanes and the electron density in the WIM lane.

4.1. Internal structure of spiral arms traced by [C II], HI, and ¹²CO

We can resolve the anatomical structure of the spiral arms, namely how each gas component is arranged spatially as a function of distance from its edges, using the velocity profiles in the tangencies. We located the peak emissions in the layers traced by [C II]–WIM component, HI (diffuse atomic clouds), ¹²CO (the GMCs), and the [C II] in molecular gas (PDRs), as indicated in the cartoon in Fig. 6, as a function of radial distance from the Galactic center. The radial distances were derived from the observed radial velocities (V_{LSR}) assuming a constant Galactic rotation speed of 220 km s⁻¹ for radius >3 kpc at the distance of these spiral arm tangencies. The Galactocentric distances derived from the V_{LSR} are listed in Table 1. The uncertainty in the Galactocentric distances, which depends on the assumed Galactic rotational speed at the tangency, does not significantly affect our results because we are only interested in the relative displacement between them. It is easy to characterize the emission profiles on the near side of the Galactic center near the tangent velocities where the emissions increase from zero. On the far side of the Galactic center, the emissions become too complex to extract the profile parameters as a result of confusion by emission from adjacent arms. This confusion is especially prominent on either side of the peak of the [C II]–WIM component. To derive the width of the emission lanes of each tracer, we therefore only used the cleaner profile on the rising portion of spiral feature on the near side to the Galactic center. We computed the Galactocentric radial distances to the V_{LSR} of peaks and the half-intensity points of each emission profile. With these radial distances, we derived the distance between the peak and half-intensity points in each emission lane. The total width was

Table 2. Derived spiral arm structure at the Perseus, Norma, and Crux tangencies.

Spiral arm	Perseus	Norma	Crux ¹
Relative lane location wrt ¹²CO (pc)			
[C II]–WIM peak	–190	–190	–600
HI peak	–20	–25	–180
Emission lane width² (pc)			
[C II]–WIM	250	270	~220
¹² CO	400	400	~440
HI	400	620	~640
Full arm width traced by [C II] and ¹² CO	480	500	~940
WIM parameters at the tangency			
Width ΔV (km s ⁻¹)	16	17	12
Intensity (K km s ⁻¹)	5.1	4.11	13.74
Path length ³ (kpc)	1.31	1.58	1.72
$\langle n(e) \rangle^4$ (cm ⁻³)	0.52	0.42	0.74

Notes. ⁽¹⁾ This longitude range is offset from the true tangency and therefore the parameters listed are only indicative of the trends within the arm structure. ⁽²⁾ FWHM as estimated using the profile on the rising side (near side to the Galactic center)–see text. ⁽³⁾ Mean path length estimated using the radial distance from the Galactic center and the width. ⁽⁴⁾ Assuming that the [C II] emission here is due to C⁺ excitation by electrons and that excitation by H atoms is negligible (cf. Velusamy et al. 2012; Velusamy & Langer 2014).

obtained by doubling this value, and the results are summarized in Tables 1 and 2.

We derive an approximate lower bound on the width for the spiral arm by assuming [C II]–WIM traces the inner edge and ¹²CO the outer edge, and we list them in Table 2. Note that in the anatomy suggested by Vallée (2014a) the hot dust emission traces the inner edge on the near side of the Galactic center with ¹²CO tracing the midplane while [C II] is in between. Using the parameters in Table 1 we sketch the cross-cut view of the spiral arm in Fig. 11. We plot each lane tracing the [C II]–WIM, HI, and molecular gas (¹²CO) by an approximate Gaussian profile. Note that we did not plot the lanes for the Crux arm because the available data do not include the main part of this tangency (see Sect. 3.3). We list the results in Table 2 as a rough estimate for this tangency because of the poor longitude coverage of the tangency. Nevertheless, the largest arm width inferred for Crux seems to be consistent with narrower widths for Perseus and Norma. The Crux spiral tangency is at the largest radial distance (~7 kpc), in contrast to ~3.5–4.5 kpc for the other arms studied here.

The cross-cut emission profiles of the internal structures (Fig. 11) for Norma and the start of the Perseus spiral arms are quite consistent with each other. The overall sizes are ~480 pc and ~500 pc for the Perseus and Norma arms, respectively. To be consistent with Vallée (2014a), we present the location of the emission lanes of [C II]–WIM and HI with respect to the location of the ¹²CO peak emission. We identify the inner edge of the arm as the location of the half power point in the [C II] emission profile on the near side of the Galactic center and on the far side from ¹²CO. Similarly, we identify the outer edge as the location of the half power point in ¹²CO emission profile on the far side from the Galactic center. We calculated the spiral arm sizes as the distance between inner and outer edges as marked in Fig. 11.

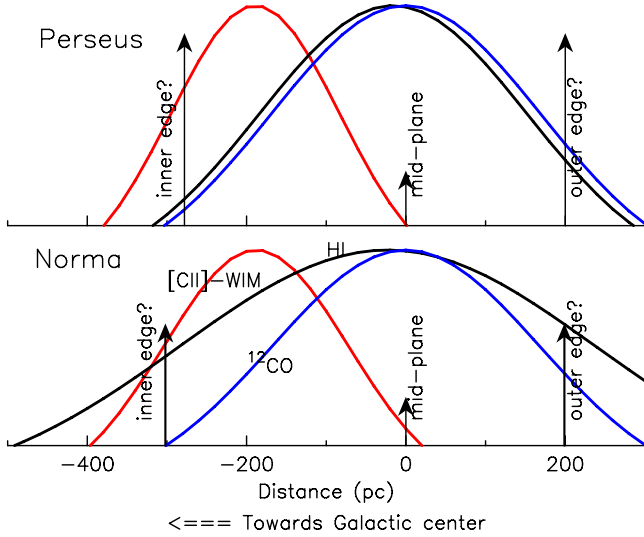


Fig. 11. Fitted spiral-arm structure of the emission lanes. Cross-cut view of the structure of the spiral arms Norma and start of Perseus are shown, including the relative locations and widths of the emission lanes. The intensity scale is arbitrary.

With the exception of the Crux arm (which also has the poor longitude coverage of the tangency in our analysis), the overall sizes are ~ 480 pc and ~ 500 pc for the Perseus and Norma arms, respectively. The similar width for these arms suggests that a width of ~ 500 pc is probably characteristic of all spiral arms in the Galaxy. Our result is close to that obtained by Vallée (2014a), who estimated a mean width ~ 600 pc for the spiral arms using the range of tangent directions observed using hot dust at the inner edge and ^{12}CO at the outer edge. Our analysis and the values for the widths presented here are likely to be less ambiguous than those of Vallée (2014a) because our data are based on fully sampled longitudinal maps in the Galactic plane observed with similar spatial and velocity resolutions. Another difference between our data and those used by Vallée (2014a) is that in his data the tangent directions were observed using maps averaged over a range of latitudes, while ours are only observed in the plane at $b = 0^\circ$.

As noted above, Vallée (2014a) constructed a cross-section view of the spiral arms that shows where each spiral arm tracer occurs. The view was based on a single value assigned for the longitude of each tangency for the tracers. This approach provided a useful insight into the different gas lanes in a cross-cut of the profile of the spiral arms. However in reality, as seen in the maps in Figs. 3 to 5, the emissions occur over a range of longitudes, and it is too complex to assign a single longitude as the tangency. In other words, all tracers have emission within a range of longitudes representing their tangency. Therefore we took a different approach to resolve and delineate the emission layers within each tangency kinematically by studying the velocity structure in each tracer spectrum. As illustrated in the cartoon of the tangency (Fig. 6), the emissions from different layers will show separate velocity V_{LSR} as a result of the Galactic rotation.

4.2. [C II] emission in the compressed WIM along the spiral arm

The spectra in Figs. 7 to 10 clearly highlight the exceptional characteristics of the [C II] emission at the tangencies. Near the extreme low velocities (near the inner edge of the spiral

arm), only [C II] shows an emission peak (representing the onset of the spiral feature) while there is little or no ^{12}CO and the HI intensity still increases with velocity. In contrast, both HI and ^{12}CO emission peaks appear at still higher velocities away from the inner edge. This anomalous excess [C II] emission in the velocity profiles is only observed for the spiral arm tangencies, where the path lengths are longest, and its detection represents the direct unambiguous identification of the large-scale Galactic diffuse ionized gas (WIM) by the $158\ \mu\text{m}$ [C II] line. The results presented here corroborate the previous detection of the WIM in the velocity-resolved HIFI data for the Scutum tangency (Velusamy et al. 2012). Our *Herschel* HIFI detection of the diffuse ionized gas provides detailed spatial and kinematic information on the nature of this gas component in the spiral arms.

It has been suggested that any contribution to the [C II] emission from excitation by H atoms is small and negligible in the WIM (Velusamy et al. 2012; Velusamy & Langer 2014). For the warm neutral medium and WIM conditions ($T_k = 8000$ K; Wolfire et al. 2003), the critical density for excitation of [C II] by H atoms is $\sim 1300\ \text{cm}^{-3}$ and for electrons it is $\sim 45\ \text{cm}^{-3}$ (see Goldsmith et al. 2012). Using the HI intensities integrated over the line width of the [C II]-WIM component and the path lengths listed in Table 2, we estimate a mean H density $\langle n(\text{H}) \rangle \sim 0.59\ \text{cm}^{-3}$ and $0.31\ \text{cm}^{-3}$ in the Perseus and Norma tangencies, respectively. As shown for the Scutum tangency (Velusamy et al. 2012), such low HI densities cannot account for the [C II] emission detected at the tangencies. Our interpretation that the [C II] emissions near the tangent velocity are the result of C^+ excitation by the collisions with electrons in the WIM and not with H atoms is further corroborated by strong evidence seen in the data presented here, as discussed above in Sect. 4.

Although the [C II] emission from the compressed WIM is observed only at or near the tangent longitudes, it is ubiquitous along the spiral arms in all directions. But, unlike the tangent direction, it is not easy to detect this enhancement in the spiral arms layers because (i) of the insufficient path length through the WIM: it is a factor of 4 to 5 shorter when viewed in any other direction than along the tangency, therefore much higher sensitivities are required to detect the weaker emission; (ii) at other longitudes, the velocities are blended with other components and it is difficult to distinguish the diffuse WIM emission from [C II] emissions from the molecular gas and PDRs due to the viewing geometry. However, it is possible to separate the emissions with spectral line data obtained with higher sensitivity and by making a spaxel-by-spaxel comparison with CO emission (e.g., Velusamy & Langer 2014). Thus, the WIM component may significantly contribute to the total [C II] luminosity in galaxies, while being difficult to detect along the average line of sight.

4.2.1. Electron densities in the spiral arm WIM

The electron density of the WIM is an important parameter for understanding the conditions in the ISM, such as the pressure and ionization rate. To estimate the electron densities required to produce the observed [C II] emission in the WIM, we followed the approach in Velusamy et al. (2012). At the low densities of the diffuse medium, the excitation is subthermal and the emission is optically thin, therefore the intensity in an ionized gas is given by (see Velusamy et al. 2012)

$$\langle n(e) \rangle \sim 0.27 T_3^{0.18} (I([\text{C II}])/L_{\text{kpc}})^{0.5}, \quad (1)$$

which assumes a fully ionized gas, a fractional abundance of C⁺ with respect to the total hydrogen density, n_t , $X(\text{C}^+) = 1.4 \times 10^{-4}$, and where L_{kpc} is the path length in kpc, T_3 is the kinetic temperature in 10^3 Kelvin, and

$$I([\text{C II}]) = \int T_A([\text{C II}]) dv \quad (2)$$

is the intensity in K km s^{-1} . The [C II] intensities given in Table 2 are integrated over the velocity widths for the [C II]–WIM profiles. The path lengths listed in Table 2 are derived using the Galactocentric radial distance and the thickness of the [C II] emission layer, as discussed above, assuming approximately circular geometry at the tangencies.

Using this approach and assuming a fully ionized gas and a fractional abundance $x(e) = n(e)/n_t = 1$, we calculated $\langle n(e) \rangle$ for all three tangencies and found $\langle n(e) \rangle$ in the range 0.42 to 0.74 cm^{-3} (see Table 2) for $T_k = 8000 \text{ K}$. For a fully ionized gas this implies a total density $n(\text{H}^+) = n(e)$. These values are strictly a lower limit if the gas is partially ionized, $x(e) < 1$, but only weakly so. The densities in the WIM at the leading edge of the spiral arms are an order of magnitude higher than the average density in the disk, which is dominated by the interarm gas. Our determination of the WIM density from the [C II] emission is several times higher than the LOS-averaged densities inferred from pulsar dispersion and H α measurements, $n(e) \sim \text{few} \times 10^{-2} \text{ cm}^{-3}$ (Haffner et al. 2009), and we argue that our higher mean value is a result of compression by the WIM–spiral arm interaction.

5. Summary

We presented large-scale [C II] spectral line maps of the Galactic plane from $l = 326.6$ to 341.4 and $l = 304.9$ to 305.9 observed with *Herschel* HIFI using OTF scans. All maps are shown as longitude-velocity (l - V) maps at a latitude $b = 0^\circ.0$, except for $l = 305.7$ to 305.9 , for which $b = +0^\circ.15$. The [C II] l - V maps along with those for HI and ^{12}CO , available from southern Galactic plane surveys (Barnes et al. 2011; McClure-Griffiths et al. 2005) were used to analyze the internal structure of the spiral arms as traced by these gas layers in the Crux ($l = 304.9$ – 305.9), Norma ($l = 327^\circ$ – 329.5), and start of Perseus ($l = 336^\circ$ – 338°) tangencies. Our key results are as follows:

1. We derived the internal structure of the spiral arm features using the velocity-resolved emission profiles of [C II], HI, and ^{12}CO averaged over each tangency. These yielded the relative locations of the peak emissions of the compressed WIM, HI, and molecular gas lanes, including the PDRs, and we derived the width of each gas lane with these values.
2. We found that the [C II] emission has two components. At the extreme velocities near the tangent velocity, only [C II] shows a peak in emission, while there is little ^{12}CO and HI is weak. This [C II] component traces the compressed WIM and is displaced by about 9 km s^{-1} in V_{LSR} corresponding to $\sim 200 \text{ pc}$ toward the inner edge of the spiral arm with respect to the ^{12}CO emission. The second [C II] component is roughly coincident with ^{12}CO and traces the PDRs of the molecular gas. The WIM and molecular gas components of [C II] are distinguished kinematically (appearing at well-separated velocities around the tangent velocity). Thus, we found that in the spiral arm tangencies the [C II] spectral line data alone can be used to study the relative locations of the WIM and molecular gas PDR layers.

3. The peak velocity of the [C II]–WIM component is near the tangent velocity and corresponds to the radial distance closest to the Galactic center. Thus it is near the inner edge of the spiral arm, representing the onset of the spiral arm feature. Both HI and ^{12}CO peak emissions appear at still higher velocities, corresponding to distances away from this inner edge. The ^{12}CO profile thus defines the outer edge of the spiral arm. We derived the width of the spiral arm as the distance between the two extremes of the half-power points in the [C II]–WIM and ^{12}CO emission profiles. We estimated the spiral arm widths as $\sim 500 \text{ pc}$ near the start of the Perseus arm and for the Norma arm.
4. We interpreted the excess [C II] near the tangent velocities as compression of the WIM induced by the spiral density waves and as the innermost edge of spiral arms. We used the [C II] intensities and a radiative transfer model to determine the electron densities of the WIM traced by [C II]. The electron densities in the compressed WIM are $\sim 0.5 \text{ cm}^{-3}$, about an order of magnitude higher than the average for the disk. The enhanced electron density in the WIM is a result of compression of the WIM by the spiral density wave potential.
5. Finally, we suggested that the WIM component traced by [C II] at the spiral arm tangencies exists all along the spiral arms in all directions, but unlike in the tangent direction, it is difficult to detect because of the insufficient path length of C⁺ across the arms and because of confusion due to velocities blended with other components. Thus, the WIM component along the spiral arms may significantly contribute to the total [C II] luminosity in galaxies, while being difficult to detect along the average line of sight.

We demonstrated the usefulness of spectrally resolved *Herschel* HIFI OTF scan maps of [C II] emission in unraveling the internal structure of spiral arms using the velocity-resolved spectral line profiles at the spiral arm tangencies. Our results provide direct observational evidence of the cross-section view of the spiral arms, in contrast to the synthetic model by Vallée (2014a), who used the longitude tangents as traced by different tracers. Combining [N II] with [C II] yields additional constraints (e.g., Langer et al. 2015; Yildiz et al. 2015), and future [N II] spectral line maps of the spiral arms are needed to fully characterize the compressed WIM detected here and the Galactic arm–interarm interactions.

Acknowledgements. We thank the staffs of the ESA *Herschel* Science Centre and NASA *Herschel* Science Center, and the HIFI, Instrument Control Centre (ICC) for their help with the data reduction routines. In addition, we owe special thanks to David Teyssier for clarifications regarding the *hebCorrection* tool. This work was performed at the Jet Propulsion Laboratory, California Institute of Technology, under contract with the National Aeronautics and Space Administration.

References

- Alves, M. I. R., Calabretta, M., Davies, R. D., et al. 2015, *MNRAS*, **450**, 2025
 Anderson, L. D., Bania, T. M., Jackson, J. M., et al. 2009, *ApJS*, **181**, 255
 Barnes, P. J., Yonekura, Y., Fukui, Y., et al. 2011, *ApJS*, **196**, 12
 Benjamin, R. A. 2008, *Massive Star Formation: Observations Confront Theory*, eds. H. Beuther, H. Linz, & T. Henning, *ASP Conf. Ser.*, **387**, 375
 Benjamin, R. A. 2009, in *IAU Symp.* 254, eds. J. Andersen, J. Bland-Hawthorn, & B. Nordström, 319
 Benjamin, R. A., Churchwell, E., Babler, B. L., et al. 2005, *ApJ*, **630**, L149
 Beuther, H., Tackenberg, J., Linz, H., et al. 2012, *ApJ*, **747**, 43
 Bloemen, J. B. G. M., Deul, E. R., & Thaddeus, P. 1990, *A&A*, **233**, 437
 Bronfman, L., May, J., & Luna, A. 2000, *Imaging at Radio through Submillimeter Wavelengths*, eds. J. G. Mangum, & S. J. E. Radford, *ASP Conf. Ser.*, **217**, 66

- Brown, J. C., Haverkorn, M., Gaensler, B. M., et al. 2007, *ApJ*, **663**, 258
- Churchwell, E., Babler, B. L., Meade, M. R., et al. 2009, *PASP*, **121**, 213
- Downes, D., Wilson, T. L., Bieging, J., & Wink, J. 1980, *A&AS*, **40**, 379
- Drimmel, R. 2000, *A&A*, **358**, L13
- Englmaier, P., & Gerhard, O. 1999, *MNRAS*, **304**, 512
- García, P., Bronfman, L., Nyman, L.-Å., Dame, T. M., & Luna, A. 2014, *ApJS*, **212**, 2
- Goldsmith, P. F., Langer, W. D., Pineda, J. L., & Velusamy, T. 2012, *ApJS*, **203**, 13
- Green, J. A., Caswell, J. L., McClure-Griffiths, N. M., et al. 2011, *ApJ*, **733**, 27
- Haffner, L. M., Dettmar, R.-J., Beckman, J. E., et al. 2009, *Rev. Mod. Phys.*, **81**, 969
- Ladd, N., Purcell, C., Wong, T., & Robertson, S. 2005, *PASA*, **22**, 62
- Langer, W. D., Velusamy, T., Pineda, J. L., et al. 2010, *A&A*, **521**, L17
- Langer, W. D., Velusamy, T., Pineda, J. L., Willacy, K., & Goldsmith, P. F. 2014, *A&A*, **561**, A122
- Langer, W. D., Goldsmith, P. F., Pineda, J. L., et al. 2015, *A&A*, **576**, A1
- Levine, E. S., Heiles, C., & Blitz, L. 2008, *ApJ*, **679**, 1288
- Mangum, J. G., Emerson, D. T., & Greisen, E. W. 2007, *A&A*, **474**, 679
- McClure-Griffiths, N., Dickey, J., Gaensler, B., et al. 2005, *ApJS*, **158**, 178
- McClure-Griffiths, N. M., & Dickey, J. M. 2007, *ApJ*, **671**, 427
- Pineda, J. L., Langer, W. D., Velusamy, T., & Goldsmith, P. F. 2013, *A&A*, **554**, A103
- Russeil, D. 2003, *A&A*, **397**, 133
- Steiman-Cameron, T. Y., Wolfire, M., & Hollenbach, D. 2010, *ApJ*, **722**, 1460
- Vallée, J. P. 2008, *AJ*, **135**, 1301
- Vallée, J. P. 2013, *Int. J. Astron. Astrophys.*, **3**, 20
- Vallée, J. P. 2014a, *ApJS*, **215**, 1
- Vallée, J. P. 2014b, *MNRAS*, **442**, 2993
- Vallée, J. P. 2014c, *AJ*, **148**, 5
- Velusamy, T., & Langer, W. D. 2014, *A&A*, **572**, A45
- Velusamy, T., Langer, W. D., Pineda, J. L., & Goldsmith, P. F. 2012, *A&A*, **541**, L10
- Wolfire, M. G., McKee, C. F., Hollenbach, D., & Tielens, A. G. G. M. 2003, *ApJ*, **587**, 278
- Yildiz, U., Goldsmith, P., Pineda, J., & Langer, W. 2015, *Am. Astron. Soc. Meet. Abstr.*, **225**, 451.09